

Algorithm Theoretical Basis Document for Land Surface Temperature (LST)

PRODUCTS: LSA-002 (ELST)

DOCUMENT SIGNATURE TABLE

| | Name | Date | Signature |
|----------------------|--|------|-----------|
| Prepared by : | I. Trigo, S. Freitas, J. Bioucas-Dias, C. Barroso, I. Monteiro, P. Viterbo, J.P. Martins | | |
| Approved by: | Land SAF Project Manager (IPMA) | | |

DOCUMENTATION CHANGE RECORD

| Issue / Revision | Date | Description: |
|------------------|------------|--|
| Version 1.0 | 19/06/2009 | Update of LST uncertainty estimations |
| Version 1.1 | 8/04/2016 | Include reference to LSA-050: re-processed SEVIRI LST product. Refer LSA-002 |
| Version 1.2 | 28/10/2016 | Modifications suggested in ORR_EPS: - Algorithm for AVHRR/Metop LST and SEVIRI/MSG LST described in separated documents. - Added note on large scale systematic uncertainties possibly affecting LST products (last paragraph of section 4.5). - Reference to snow/ice emissivity included in section 4.3. - Improved description of ELST re-gridding procedure (end of section 5). - Clarified that only the primary satellite is used (1st paragraph in section 1). |
| Issue 2 | 02/06/2017 | Added annex with description of Processing Scheme (removed from product PUM). |

DISTRIBUTION LIST

| Internal Consortium Distribution | | |
|---|------------------------|-------------------|
| Organisation | Name | No. Copies |
| IPMA | Isabel Trigo | |
| IPMA | Isabel Monteiro | |
| | | |
| IDL | Carlos da Camara | |
| IPMA | Sandra Coelho | |
| IPMA | Carla Barroso | |
| IPMA | Pedro Diegues | |
| IPMA | Teresa Calado | |
| IPMA | Pedro Ferreira | |
| IPMA | Ricardo Torres | |
| IMK | Folke-S. Olesen | |
| IMK | Frank Goettsche | |
| IMK | Ewa Kabsch | |
| MF | Jean-Louis Roujean | |
| MF | Dominique Carrer | |
| MF | Dominique Carrer | |
| RMI | Françoise Meulenberghs | |
| RMI | Arboleda Alirio | |
| RMI | Nicolas Ghilain | |
| FMI | Niilo Siljamo | |
| UV | Joaquin Melia | |
| UV | F. Javier García Haro | |
| UV/EOLAB | Fernando Camacho | |
| UV | Alexander Verger | |

| External Distribution | | |
|------------------------------|-------------------|-------------------|
| Organisation | Name | No. Copies |
| EUMETSAT | Frédéric Gasiglia | |
| EUMETSAT | Cleber Balan | |
| EUMETSAT | Lorenzo Sarlo | |
| EUMETSAT | Lothar Schueller | |
| EDISOFT | Tiago Sepúlveda | |
| EDISOFT | Joana Rosa | |
| EDISOFT | Joaquim Araujo | |
| GMV | Mauro Lima | |
| | | |

| Steering Group Distribution | | |
|------------------------------------|-----------------------|-------------------|
| Nominated by: | Name | No. Copies |
| IPMA | Pedro Viterbo | |
| EUMETSAT | Lothar Schüller | |
| EUMETSAT | Jörg Ackermann | |
| EUMETSAT | Harald Rothfuss | |
| STG/AFG (USAM) | Piotr Struzik | |
| MF | Jean-François Mahfouf | |
| RMI | Rafiq Hamdi | |
| KIT | Jan Cermak | |
| VITO | Bart Deronde | |

Table of Contents

| | |
|---|----|
| DOCUMENT SIGNATURE TABLE | 2 |
| DOCUMENTATION CHANGE RECORD | 2 |
| 1. Introduction | 7 |
| 2. Data Description | 8 |
| 2.1. AVHRR on-board Metop | 8 |
| 2.2. Calibration/Verification Database | 8 |
| 2.3. Radiative Transfer Simulations | 10 |
| 3. The Land-SAF ELST Algorithm | 11 |
| 3.1. Generalized Split-Windows | 11 |
| 3.2. Calibration/Validation of the GSW Algorithm | 12 |
| 4. Error Propagation | 13 |
| 4.1. Framework | 13 |
| 4.2. Impact of Sensor Noise | 15 |
| 4.3. Impact of uncertainties in Surface Emissivity | 15 |
| 4.4. Uncertainties in forecasts of atmospheric water vapour content | 16 |
| 4.5. Uncertainty of LST Retrievals | 17 |
| 5. Daily Composites of AVHRR/Metop LST – LSA-002 | 18 |
| 6. Concluding Remarks | 19 |
| 7. References | 21 |
| Annex AVHRR/MetOp LST Product: LSA-002 (ELST) | |

List of Tables

| | |
|--|----|
| Table 1 Central wavenumber and band-correction coefficients for AVHRR thermal windows channels onboard Metop-A and Metop-B, respectively (EUMETSAT, 2011). | 11 |
| Table 2 Uncertainty values considered for surface emissivity of Metop channels 4 and 5. | 16 |
| Table 3 Fraction of Vegetation Cover attributed per land cover class. | 18 |
| Table 4- Description of LST/AVHRR Quality Flag information. | 19 |

List of Figures

| | |
|---|----|
| Figure 1 Spectral response functions of AVHRR thermal windows channels (5 and 4), centred at 10.8 and 11.9 μm , respectively, on-board Metop1 and Metop2. | 8 |
| Figure 2 Main properties of the calibration database for AVHRR/Metop LST: a) TCWV distribution, b) T_Skin distribution, c) Bivariate TCWV/T_Skin distribution and d) geographical distribution. | 9 |
| Figure 3 Assessment of the ELST Generalized Split-Windows algorithm against the validation databased: root mean square differences ($^{\circ}\text{C}$) per classes of Total Column Water vapour (x-axis) and view zenith angle (y-axis), considering the coefficients calibrated for Metop-A and Metop-B response functions, respectively. | 12 |
| Figure 4 Uncertainty in LST estimates, measured as the RMSD ($^{\circ}\text{C}$) between retrieved LST and the validation database true value, considering: (a) the input data are error-free; (b) the sensor noise; (c) the uncertainty associated to total column water vapour forecasts; (d) uncertainty in surface emissivity, for cases where it lies between 0.8 and 0.95 (mostly barren surfaces); (e) uncertainty in surface emissivity, for cases where it lies between 0.95 and 0.98 (sparsely to moderately vegetated surfaces); (f) uncertainty in surface emissivity, for cases where it is higher than 0.95 (vegetated and/or moist surfaces or inland water bodies). The lower row represents total uncertainty, for the emissivity types described above. The results are presented for combinations of W (x-axis) and view zenith angle (y-axis), for Metop-B algorithm. | 14 |
| Figure 8 Example of one Daytime LST estimate ($^{\circ}\text{C}$) and respective quality flag. | 20 |
| Figure 9 Example of one Night-time LST estimate ($^{\circ}\text{C}$) and respective quality flag. | 21 |
| Figure 6 - Diagram of processing chain for AVHRR/Metop retrieved EM (left) and LST (right). | 26 |

1. Introduction

This document details the algorithm used for the retrieval of Land Surface Temperature (LST) from the Advanced Very High Resolution Radiometer (AVHRR) on-board EUMETSAT polar system satellites, the Metop series. The methodology detailed here applies to daily AVHRR LST product (LSA-002), following a very similar algorithm to that used for LSA SAF LST product derived from Meteosat Second Generation (with product identifiers LSA-001 and LSA-050). The LSA SAF ELST product is generated from observations gathered by the primary Metop satellite.

LST estimations from remotely sensed data are generally obtained from one or more channels within the thermal infrared atmospheric window from 8-to-13 μm (Dashet al., 2002). Operational LST retrievals often make use of split-window algorithms (e.g., Prata, 1993; Wan and Dozier, 1996), where LST is obtained through a semi-empirical regression of top-of-atmosphere (TOA) brightness temperatures of two pseudo-contiguous channels, i.e., the split-window channels. The Land-SAF LST algorithm is based on the generalised split-window (GSW) formulation initially developed for AVHRR and MODIS (Wan and Dozier, 1996), recalibrated taking into account AVHRR-3 channels. The error of LST retrievals via GSW depends on (i) the uncertainty of surface emissivity, (ii) the water vapour content of the atmosphere, and (iii) or the satellite view angle. Because the latter determines the total optical path, LST estimations are often limited to satellite zenith angles (SZA) below $\sim 60^\circ$, where retrieval errors are still acceptable (e.g., Wan and Dozier, 1996; Sun and Pinker, 2003; Jiménez-Muñoz and Sobrino, 2006; Freitas et al., 2011; Martins et al, 2016). The LSA SAF AVHRR/Metop product is generated globally, for satellite zenith angles up to 60° .

2. Data Description

2.1. AVHRR on-board Metop

Metop satellites constitute the current EUMETSAT polar system and amongst others, are equipped with the Advanced Very High Resolution Radiometer (AVHRR), which has a swath of about 2400km, providing Earth observations with view zenith angles (SZA) up to about 60° , and a spatial resolution at nadir of 1.1 km. AVHRR provides information on 6 channels, with two in the thermal infrared. As in the case of SEVIRI, the latter are centred at about $10.8 \mu\text{m}$ and $11.9 \mu\text{m}$ (Figure 1), respectively, and are used to derive LST.

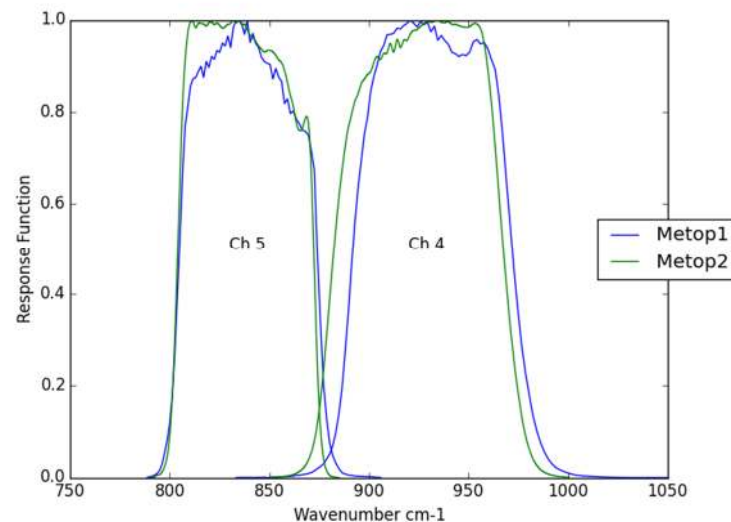


Figure 1 Spectral response functions of AVHRR thermal windows channels (5 and 4), centred at 10.8 and $11.9 \mu\text{m}$, respectively, on-board Metop1 and Metop2.

2.2. Calibration/Verification Database

The calibration (and verification) of the GSW presented here relies on radiative transfer simulations of TOA brightness temperatures for AVHRR channels 4 and 5. The simulations are performed for the database of global profiles of temperature, moisture, and ozone compiled by Borbas et al. (2005) for clear sky conditions, and referred to as SeeBor. The database contains over 15,700 profiles taken from other datasets, such as NOAA88 (Seemann et al., 2003), TIGR-like (Chevallier, 2001), and TIGR (Chedin et al., 1996), that are representative of a wide range of atmospheric (clear sky) conditions over the whole globe. In addition, surface parameters such as skin temperatures (T_{skin}) and a landcover classification within the International Geosphere-Biosphere Programme ecosystem categories (IGBP) (Belward, 1996) are assigned to each profile. Skin temperature over land surfaces corresponds to LST in SeeBor and is estimated as a function of 2m temperature ($T_{2\text{m}}$), and solar zenith and azimuth angles (Borbas et al. 2005).

The calibration database of the GSW for ELST takes into account that this is a global product. For this purpose, we consider a set of globally distributed atmospheric profiles with the properties described in Figure 3 (Martins et al., 2016). The calibration databased followed the following criteria:

- 1) First we define classes of T_{Skin} (from 200 K to 330 K in steps of 5 K) and TCWV from 0 to 6 cm in classes of 0.75 mm. A large enough number of profiles are selected from the SeeBor, ensuring that the all physically possible cases in the TCWV/ T_{Skin} phase state is fully covered (see Figure 3c).
- 2) For each of the selected profiles, we assign a new T_{Skin} based on the ranges of $T_{\text{Skin}} - T_{\text{air}}$ to cover realistic ranges. The choice of the range of perturbations to apply is key to the performance of the LST algorithms. Here we considered a range of $\pm 15\text{K}$ around T_{air} in steps of 5K.
- 3) Each of these conditions may be sensed from angles ranging from 0 (nadir view) to 60° in steps of 2.5° .
- 4) Emissivity range: values of $\epsilon_{10.8}$ (channel 4) from 0.93 to 1.0 in steps of 0.01; values of $\epsilon_{12.0}$ (channel 5) are based on departures from the former: -0.015 to 0.035 in steps of 0.01 (excluding cases where $\epsilon_{12.0} > 1$).

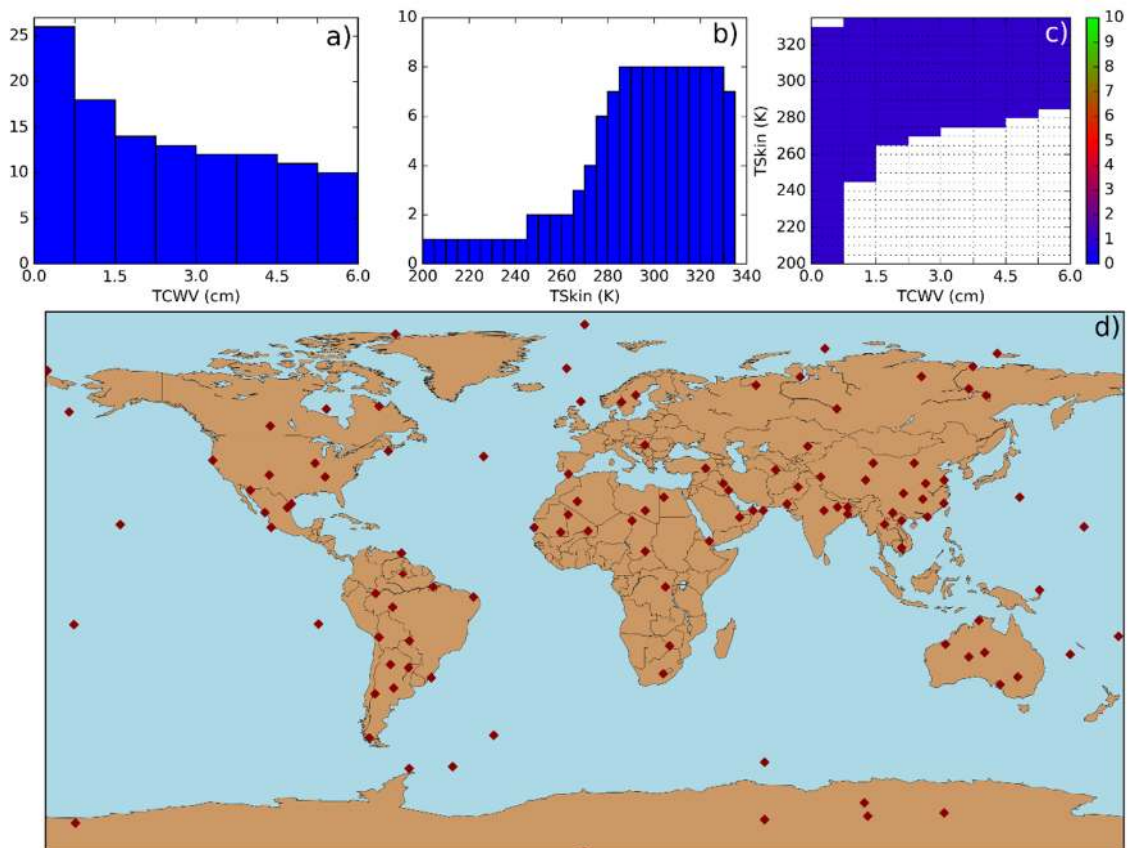


Figure 2 Main properties of the calibration database for AVHRR/Metop LST: a) TCWV distribution, b) T_{Skin} distribution, c) Bivariate TCWV/ T_{Skin} distribution and d) geographical distribution.

The spatial distribution of SeeBor profiles selected to be part of the calibration database is shown in Figure 2d. The statistical distributions of skin temperature (or surface temperature), TCWV, as well as their joint distributions are shown in Figure 2a, Figure 2b, and Figure 2c. The verification database will then be formed by all SeeBor profiles, excluding those selected for calibration purposes.

2.3. Radiative Transfer Simulations

The MODerate spectral resolution atmospheric TRANSmittance algorithm (MODTRAN4) (Berk et al., 2000) provides a useful tool to quantify the radiation emitted by the surface within known atmospheric conditions that reaches a sensor operating in a specific spectral band. The radiance (L_ν) is estimated using MODTRAN4, for the bands corresponding to AVHRR channels 4 and 5, with a spectral resolution of 1 cm^{-1} . The integration of L_ν weighted by the i -th channel response function $\phi_{i,\nu}$, (see Figure 1) provides channel i effective radiance:

$$L_i = \frac{\int_{\nu_{i,1}}^{\nu_{i,2}} \phi_{i,\nu} L_\nu d\nu}{\int_{\nu_{i,1}}^{\nu_{i,2}} \phi_{i,\nu} d\nu} \quad (1)$$

where $\nu_{i,1}$ and $\nu_{i,2}$ are the lower and upper wavenumber boundaries of the channel, respectively; the integrals in (1) are estimated taking into account the full tabulated values of the response function $\phi_{i,\nu}$, i.e., between $\nu_1 = 830 \text{ cm}^{-1}$ and $\nu_2 = 1050 \text{ cm}^{-1}$, for channel 4, and between $\nu_1 = 760 \text{ cm}^{-1}$ and $\nu_2 = 910.00 \text{ cm}^{-1}$, for channel 5.

The simulated AVHRR radiances for channel i , L_i , are then converted to equivalent black-body brightness temperatures (Tb_i) following the analytic formulation based on the Planck function (EUMETSAT, 2011):

$$Tb_i = A_i + B_i \frac{C_2 \nu_{ci}}{\ln\left(1 + \frac{C_1 \nu_{ci}^3}{L_i}\right)} \quad (2)$$

where $\nu_{i,c}$ is channel i central wavenumber (Table 1), $C_1 = 2hc^2$ and $C_2 = hc/k$ (h is the Planck constant, c the speed of light and k the Boltzmann constant). The parameters A_i and B_i , shown in Table 1 for Metop-A and Metop-B, are band-correction coefficients, adjusted to AVHRR spectral response functions. The simulations of channel 4 and channel 5 brightness temperatures are then performed for both Metop-A and Metop-B, for the whole database (calibration and verification subsets) described in the previous sections.

Table 1 Central wavenumber and band-correction coefficients for AVHRR thermal windows channels onboard Metop-A and Metop-B, respectively (EUMETSAT, 2011).

| Channel | Metop-A | | | Metop-B | | |
|-----------|-----------------------------|----------|--------|-----------------------------|----------|---------|
| | ν_c (cm ⁻¹) | A (K) | B | ν_c (cm ⁻¹) | A (K) | B |
| Channel 4 | 926.566 | -0.45749 | 1.0014 | 933.630 | -0.50487 | 1.00136 |
| Channel 5 | 836.344 | -0.13685 | 1.0007 | 839.620 | -0.38171 | 1.00114 |

3. The Land-SAF ELST Algorithm

3.1. Generalized Split-Windows

Several algorithms have been proposed to retrieve LST from remotely sensed thermal infrared data, e.g., Prata (1993), Dash et al. (2002), Sun and Pinker (2003), Sobrino and Romaguera (2004), Jiménez-Muñoz (2006), Coll et al., (2006), Yu et al. (2008), Jiang and Li (2008). The LSA SAF ELST is estimated following the same approach used for SEVIRI/MSG LST (Trigo et al., 2008b, Freitas et al., 2011, Martins et al., 2016) using a Generalized Split-Window (GSW) algorithm with a formulation similar to that first proposed by Wan and Dozier (1996) for MODIS. Thus, LST is as a function of TOA brightness temperatures of AVHRR channels 4 and 5 ($T_{10.8}$ and $T_{12.0}$, respectively):

$$LST = \left(A_1 + A_2 \frac{1-\varepsilon}{\varepsilon} + A_3 \frac{\Delta\varepsilon}{\varepsilon^2} \right) \frac{T_4 + T_5}{2} + \left(B_1 + B_2 \frac{1-\varepsilon}{\varepsilon} + B_3 \frac{\Delta\varepsilon}{\varepsilon^2} \right) \frac{T_4 - T_5}{2} + C + \Delta LST \quad (3)$$

where ε is the average of the two channels surface emissivities, $\Delta\varepsilon$ their difference ($\varepsilon_{10.8} - \varepsilon_{12.0}$), while A_j , B_j , ($j = 1,2,3$) and C are the GSW coefficients obtained by fitting equation (3) to the calibration data described above, and ΔLST is the model error; for each class of water vapour W and SZA Ψ , a set of coefficients A_j , B_j , C is inferred by minimizing the the l_2 -norm of the model error ΔLST . The GSW algorithm is applied to clear sky pixels only. In the Land-SAF, cloud removal is performed using the software developed by the Nowcasting (NWC) SAF, which is based on multispectral threshold technique applied to visible, near-infrared, and thermal atmospheric window AVHRR channels, for each pixel of the image (Dybbroe et al, 2005).

A relevant factor in the selection of the algorithm was its expected reliability for operational LST retrievals, both in terms of expected accuracy and timeliness. The latter favours the use of semi-empirical relationships between LST and TOA brightness temperatures, which are computationally efficient and free of the convergence problems of direct emissivity and temperature retrieval methods (e.g., Faysash and Smith, 1999, Masiello et al., 2015) associated to the non-linearity of the inverse problem in remote sensing (e.g., Rodgers, 2000).

3.2. Calibration/Validation of the GSW Algorithm

The GSW parameters A_i , B_i , and C obtained by fitting equation (3) to the calibration dataset described in section 2.2. The GSW algorithm is verified against the independent subset of simulated TOA brightness temperatures comprised of all SeaWiFS profiles except for those selected for calibration (section 2.2). Figure 3 shows the error distribution of GSW LST models calibrated for Metop-A and Metop-B, respectively, within each class of W and SZA.

The overall bias of the GSW is -0.196°C for Metop-A and -0.193°C for Metop-B, while RMSE values are 0.553°C and 0.541°C for Metop-A and Metop-B, respectively. As shown in Figure 3, the retrieval errors tend to increase with both SZA and W. The RMSE is always below 2K for water vapour content and angles within the range of values admissible for Land-SAF ELST estimations, except for a few extreme cases with total column of water in the atmosphere close to 60 mm and view zenith angle at the edge of AVHRR swath.

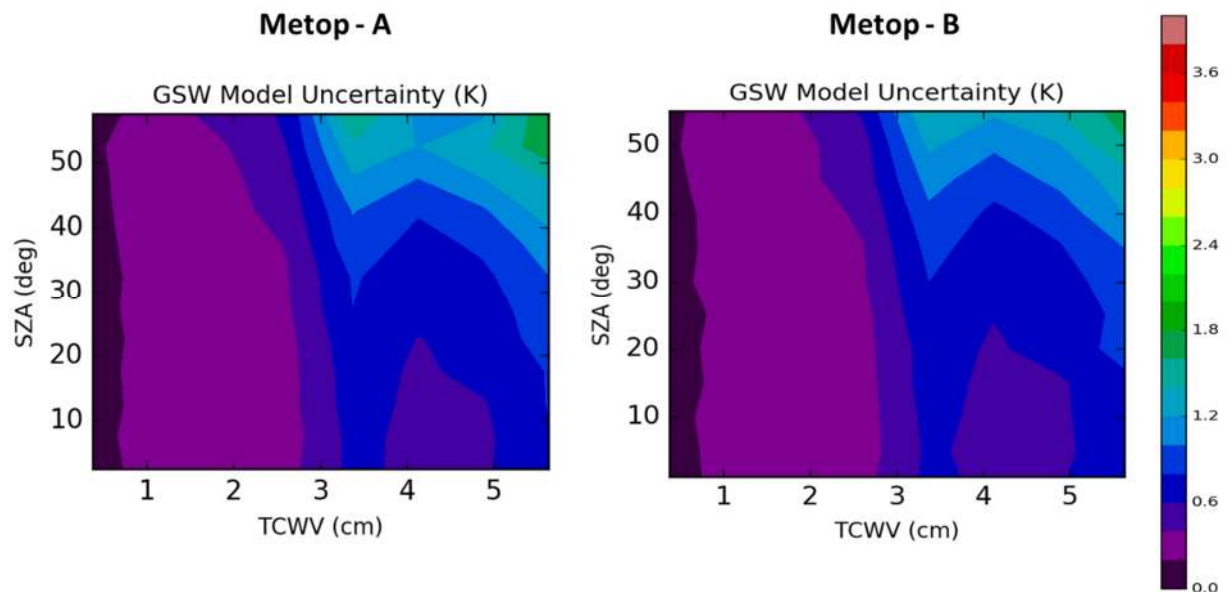


Figure 3 Assessment of the ELST Generalized Split-Windows algorithm against the validation databased: root mean square differences ($^{\circ}\text{C}$) per classes of Total Column Water vapour (x-axis) and view zenith angle (y-axis), considering the coefficients calibrated for Metop-A and Metop-B response functions, respectively.

4. Error Propagation

In a real scenario, we do not have access to the exact GSW inputs $X = (T_{10.8}, T_{12.0}, \varepsilon_{10.8}, \varepsilon_{12.0})$ and $Y = (W, \Psi)$, but only to inaccurate inputs, which we denote by $\hat{X} = (\hat{T}_{10.8}, \hat{T}_{12.0}, \hat{\varepsilon}_{10.8}, \hat{\varepsilon}_{12.0})$ and $\hat{Y} = (\hat{W}, \hat{\Psi})$. Therefore, if we still infer the LST according to model (3) replacing the exact GSW inputs with the inaccurate ones, we have a new source of error on the top of the fitting error ΔLST shown in Figure 3. In the current section, the main errors sources are identified and their impact on the total LST error estimated.

Potentially, all inputs may introduce errors in retrieved LST values. However, here we only consider the radiometric noise, the uncertainty in surface emissivity and errors in W forecasts. The misclassification of cloudy pixels as clear sky has very high impact on the retrieved LST. It is very difficult to propagate the uncertainty in cloud identification to LST uncertainty. Instead, users are recommended to be wary of LST retrievals in neighbouring cloudy pixels.

4.1. Framework

Let us define the vector of model coefficients $\theta = (A_1, A_2, A_3, B_1, B_2, B_3, C)$. Notice that, the vector θ generated by the fitting process is a function of water content and view angle, i.e., $\theta = \theta(Y)$. Consider the LST estimator $L\hat{S}T = f(\hat{X}, \hat{\theta})$ where $\hat{\theta} = \theta(\hat{Y})$ and $f(X, \theta)$ is the LST estimate given by model (3). A characterization of the model error is given by:

$$S_{LST} = E \left[\left(f(\hat{X}, \hat{\theta}) - LST \right)^2 \mid X, Y \right]^{1/2} \quad (4)$$

where $E[\cdot \mid X, Y]$ stands for mean value conditioned to X and Y ; i.e., for a given GSW input X, Y , we want to compute the RMSE of the LST estimate. Using the fact that $LST = f(X, \theta) + \Delta LST$ and assuming that $E[f(\hat{X}, \hat{\theta}) \mid X, Y] = f(X, \theta)$, we may write:

$$S_{LST}^2 = E \left[\left(f(\hat{X}, \hat{\theta}) - f(X, \theta) \right)^2 \mid X, Y \right] + \Delta LST^2 \quad (5)$$

By taking a linear approximation of $f(\hat{X}, \hat{\theta})$ in the neighbourhood of (X, θ) , and denoting $\sigma_{X_i}^2 = E \left[\left(\hat{X}_i - X_i \right)^2 \mid X \right]$ and $\sigma_{\theta_i}^2 = E \left[\left(\hat{\theta}_i - \theta_i \right)^2 \mid Y \right]$, we are led to

$$S_{LST}^2 = \sum_i \left(\frac{\partial f}{\partial X_i} \right)^2 \sigma_{X_i}^2 + \sum_j \left(\frac{\partial f}{\partial \theta_j} \right)^2 \sigma_{\theta_j}^2 + \Delta LST^2, \quad (6)$$

where we have assumed that the components of X , Y are mutually independent and that $E[(\hat{X}_i - X_i) | X] = 0$ and $E[(\hat{\theta}_i - \theta_i) | Y] = 0$. Next, we study in detail the error due to each individual GSW input.

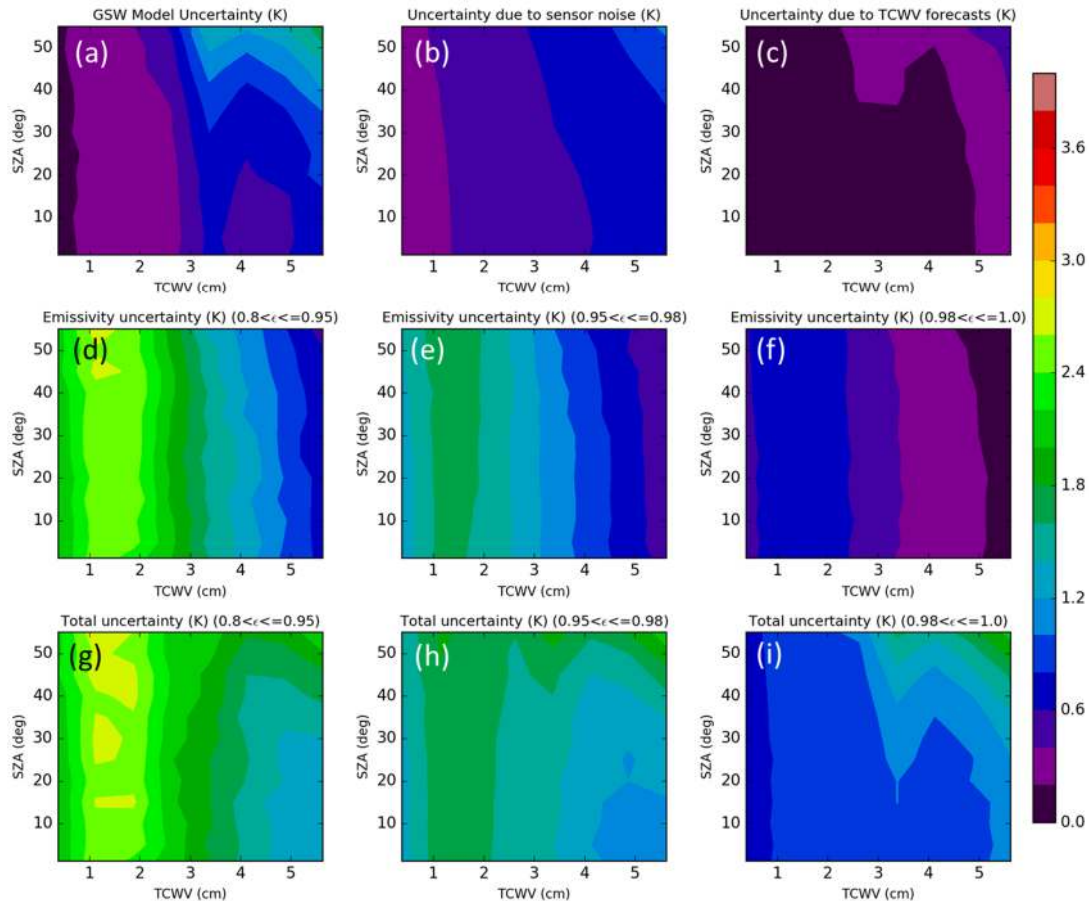


Figure 4 Uncertainty in LST estimates, measured as the RMSD ($^{\circ}\text{C}$) between retrieved LST and the validation database true value, considering: (a) the input data are error-free; (b) the sensor noise; (c) the uncertainty associated to total column water vapour forecasts; (d) uncertainty in surface emissivity, for cases where it lies between 0.8 and 0.95 (mostly barren surfaces); (e) uncertainty in surface emissivity, for cases where it lies between 0.95 and 0.98 (sparsely to moderately vegetated surfaces); (f) uncertainty in surface emissivity, for cases where it is higher than 0.95 (vegetated and/or moist surfaces or inland water bodies). The lower row represents total uncertainty, for the emissivity types described above. The results are presented for combinations of W (x-axis) and view zenith angle (y-axis), for Metop-B algorithm.

4.2. Impact of Sensor Noise

The expected radiometric noise of AVHRR channels 4 and 5 on-board Metop series is set 0.12°C. The associated LST uncertainty is then

$$S_{Tb}^2 = S_{Tb4}^2 + S_{Tb5}^2 \quad (7)$$

where

$$S_{Tb4}^2 = \left(\frac{\partial f}{\partial T_4} \right)^2 \sigma_{T_4}^2 \quad \text{and} \quad S_{Tb5}^2 = \left(\frac{\partial f}{\partial T_5} \right)^2 \sigma_{T_5}^2 \quad (8)$$

Figure 4b shows the distributions of errors attributed to the impact of sensor noise, S_{Tb} , grouping all possible SZA within different ranges of W. S_{Tb} is generally below 0.8°C, and increases with the atmospheric water content.

4.3. Impact of uncertainties in Surface Emissivity

The impact of uncertainties in surface emissivity for channels 4 and 5, $\sigma_{\varepsilon 4}$ and $\sigma_{\varepsilon 5}$, respectively, on LST is given by:

$$S_{\varepsilon}^2 = S_{\varepsilon 4}^2 + S_{\varepsilon 5}^2 \quad (9)$$

where

$$S_{\varepsilon 4}^2 = \left(\frac{\partial f}{\partial \varepsilon_4} \right)^2 \sigma_{\varepsilon 4}^2 \quad \text{and} \quad S_{\varepsilon 5}^2 = \left(\frac{\partial f}{\partial \varepsilon_5} \right)^2 \sigma_{\varepsilon 5}^2. \quad (10)$$

Emissivity retrievals are based on the so-called Vegetation Cover Method (Caselles and Sobrino, 1989; Peres and DaCamara, 2005), where effective channel emissivity for any given pixel is estimated as a weighted average of channel emissivities of dominant bareground and vegetation types within the scene. Furthermore, it is considered that AVHRR pixels may include a land, F_{Land} , and an in-land water fraction ($1 - F_{Land}$), and thus the effective pixel emissivity, ε_{eff_IRn} , is given by:

$$\varepsilon_{LAND_n} = \varepsilon_{veg_n} FVC + \varepsilon_{bg_n} (1 - FVC) \quad (11a)$$

$$\varepsilon_{eff_n} = \varepsilon_{LAND_n} F_{Land} + \varepsilon_{WATER_n} (1 - F_{Land}) \quad (11b)$$

where FVC is the pixel fraction of vegetation cover and ε_{veg_n} , ε_{bg_n} , ε_{WATER_n} are the vegetation, bareground, and water emissivities, respectively, for the split-window channel n . The values for ε_{veg_n} and ε_{bg_n} are available from look-up-tables, determined for the land cover classes within the IGBP (Belward, 1996) database (Peres and DaCamara, 2005); in the case of inland water, ε_{WATER_IRn} is set to the Water Bodies values, while pixels identified as snow/ice (either by the cloud mask algorithm or by the H-SAF snow products) are also set to the respective emissivity tabulated values. Channel emissivity is

to be estimated from FVC retrieved by the Land-SAF from AVHRR/Metop. It is however set to constant until this product is implemented in the production chain (see Table 3).

The uncertainties in retrieved emissivity are thoroughly discussed in (Trigo et al, 2008a). Emissivity uncertainties are higher for low emissivity surfaces (barre ground) and low for high emissivity surfaces (densely vegetated or water surfaces). The assessment of the impact assumed the following uncertainty values in surface emissivity (Table 2), estimated taking into account the variability of ε_4 and ε_5 , as compiled from spectral databases (see Trigo et al., 2008a).

Table 2 Uncertainty values considered for surface emissivity of Metop channels 4 and 5.

| Emissivity Ranges | Channel 4 σ_{ε_4} | Channel 5 σ_{ε_5} |
|--------------------------------|--|--|
| $\varepsilon < 0.95$ | 0.030 | 0.025 |
| $0.95 \leq \varepsilon < 0.98$ | 0.020 | 0.010 |
| $\varepsilon \geq 0.98$ | 0.006 | 0.006 |

Figure 4d, Figure 4e and Figure 4f show the results obtained for different ranges of surface emissivity. The results are shown taking into account the total column water vapour and satellite zenith angle. As expected, the sensitivity to land surface emissivity is significantly higher for drier atmospheres, since under moist conditions the impact of emissivity on the surface emitted radiance is partially compensated by an opposite effect on the (higher) atmospheric radiation reflected by the surface (Trigo et al., 2008a). Moreover, the higher values of σ_{ε_4} and σ_{ε_5} are found in (semi-)arid regions (Table 2), leading to LST inaccuracies of 1°C or more under dry conditions (W below 2 cm). In contrast the impact on LST is always below 1.6°C for the moister atmospheres ($W > 4.5$ cm).

4.4. Uncertainties in forecasts of atmospheric water vapour content

According to the equation (6), the error due to uncertainties in the water vapour content is given by:

$$S_W^2 = \sum_j \left(\frac{\partial f}{\partial \theta_j} \right)^2 \sigma_{\theta_j}^2 \quad (12)$$

where

$$\sigma_{\theta_j}^2 = E \left[\left(\hat{\theta}_j - \theta_j \right)^2 \mid W, \Psi \right] \quad (13)$$

Since we neglect the uncertainty in the SZA Ψ , let us focus out attention on W . Given that $\hat{\theta}$ is a piece-wise linear function, we have

$$\sigma_{\theta_j}^2 = E \left[\left(\hat{\theta}_j - \theta_j \right)^2 \mid W \right] = \sum_k \left(\hat{\theta}_j(R_k) - \theta_j \right)^2 P(\hat{W} \in R_k \mid W) \quad (14)$$

where R_k is the region of the water vapour domain where the k-th linear model is assumed. Therefore the sets R_k are a partition of the referred to domain.

The operational use of the GSW algorithm (3) to retrieve LST from AVHRR makes use of forecasts of total column water vapour (W) provided by the European Centre for Medium-range Weather Forecasts (ECMWF), for parameter selection. To characterize W error statistics, we compare ECMWF W forecasts (with forecast steps ranging between 12 and 36 h) with the respective analysis, for the 15th of each month for 1 full year, excluding cases with model cloud cover higher than 10%. This exercise is regularly (about once per year) to update the uncertainty in ECMWF forecasts.

The comparison between W forecasts and analysis (the reference value) allows us to estimate the probability $P(\hat{W}_i | W_j)$, i.e., the probability that \hat{W} belongs to the water vapour content class W_i , given that the true class is W_j . This probability is then used to compute the expected LST error, according to the expressions (12) to (14). Figure 4c shows the impact on LST retrievals, which is exclusively attributed to forecast errors. These are generally very low, although they show an increase with the atmospheric moisture content.

4.5. Uncertainty of LST Retrievals

The estimation of LST error bars, S_{LST} , assumes that all sources of errors described in the previous sections are independent:

$$S_{LST} = \sqrt{S_{Tb}^2 + S_{\varepsilon}^2 + S_w^2 + \Delta LST^2} \quad (15)$$

Figure 4g, Figure 4h, and Figure 4i show the total uncertainty of LST for different scenarios of surface emissivity (and respective uncertainties). These were obtained for “LST retrievals” computed for the validation dataset described in section 2.2 and taking into account the uncertainties of the different input variables, as discussed above. Dry atmospheres present the widest range of S_{LST} in the case the surface emissivity is also low. Under such conditions, the total error depends essentially on emissivity uncertainties and to a lesser extent on the view zenith angle. For the case of high emissivity surfaces, S_{LST} increase with total water vapour content and view angle, i.e., LST error bars increase for higher optical depths.

The ELST product will be affected by large-scale systematic uncertainties. However, it should be stressed that the most likely source of systematic uncertainties in the LSA SAF LST products arises from systematic errors in surface emissivity. Given its low variability in time, errors in the bareground or vegetation emissivity attributed to any given pixel translates into a source of systematic errors, particularly relevant in arid and sparsely vegetated regions.

5. Daily Composites of AVHRR/Metop LST – LSA-002

The LSA SAF AVHRR/Metop LST product (ELST, product identifier LSA-002) consists of daily composites of LST values retrieved from individual AVHRR/Metop from individual Product Distribution Units, PDUs. The generalized split-window algorithm described above is applied to channel 4 and 5 top-of-atmosphere brightness temperatures, as described in the previous sections. Since the Fraction of Vegetation Cover (FVC) product based on AVHRR/Metop data has not yet been implemented, the current version of PDU-based LST is using a static emissivity map. This in turn is based on the land-cover classification of each pixel, according to the IGBP database, and on an average (fixed) value of the Fraction of Vegetation Cover attributed to each class following Peres and DaCamara (2005) (Table 3). The FVC values fixed in Table 3 are currently being used as input for the vegetation cover method used in the AVHRR/Metop LST processing, and will be replaced by the 10-daily LSA SAF FVC product which is planned to be derived from AVHRR (end of 2016).

Table 3 Fraction of Vegetation Cover attributed per land cover class.

| IGBP Land Cover Class | Fraction of Vegetation Cover |
|----------------------------------|-------------------------------------|
| 1 – Evergreen Needle-leaf forest | |
| 2 – Evergreen Broad-leaf forest | |
| 3 – Deciduous Needle-leaf forest | 0.8 |
| 4 – Deciduous Broad-leaf forest | |
| 5 – Mixed Forest | |
| 6 – Closed Shrubs | |
| 7 – Open Shrubs | |
| 8 – Woody Savannah | |
| 9 – Savannah | 0.5 |
| 10 – Grasslands | |
| 12 – Croplands | |
| 14- Crops / Natural Vegetation | |
| 11 – Wetlands | |
| 15 – Snow/ ice | 0 |
| 17 – water bodies | |
| 13 – Urban | 0.1 |
| 16 – Barren | 0.005 |

The estimation of LST uncertainty (error-bars) following the procedure described in section 4 will be implemented for the LST_AVHRR product only after the AVHRR/Metop FVC product is integrated into the LSA SAF system and the complete error propagation analysis described therein can be performed. At the moment, the LST_AVHRR (ELST, LSA-002) is distributed with a quality flag (Table 4), where providing qualitative information on the product quality. Taking into account the analysis of error propagation within the verification dataset, and the actual retrieval conditions (in terms of atmospheric moisture, viewing angle, and land-cover/emissivity), LST estimates are considered to be:

- Nominal when similar to conditions in validation database yield LST uncertainties between 1°C and 2°C.

- Below nominal when similar to conditions in validation database yield LST uncertainties above 2°C.
- Above nominal when similar to conditions in validation database yield LST uncertainties below 1°C.

Table 4- Description of LST/AVHRR Quality Flag information

| Decimal Value | Description |
|----------------------|------------------------------------|
| -5 | CMA - contaminated by snow/ice |
| -4 | CMA - Cloud filled |
| -3 | CMA - pixel contaminated by clouds |
| -2 | Viewing Angle Out of Range |
| -1 | Sea Pixel |
| 0 | Unprocessed pixel |
| 1 | Below Nominal |
| 2 | Nominal |
| 3 | Above Nominal |

The PDU-based LST estimates are then organized by night-time and daytime values, according to the respective solar zenith angle (above or below 90° for night-time or daytime, respectively) and projected over a sinusoidal grid centred at (0°N,0°W), with a resolution of 0.01° by 0.01°. The projection to the sinusoidal grid is performed according to the following procedure:

1) we compute the location of the AVHRR/Metop pixel in the sinusoidal grid, ensuring that daytime and night-time AVHRR observations are treated separately.

2) we then consider all AVHRR LST pixels falling in the same grid-cell and the final LST value (as well as observation time and view zenith angle) will correspond to an average of all valid points; the QF will be set to the "worst" class; the number of original PDU pixels overlapping each sinusoidal grid-box is also provided

3) to avoid systematic gaps in the sinusoidal grid, we do a final check for non-filled grid cells; if these do not correspond to identified clouds/ sea pixels, they are filled in with an average of neighbouring points.

6. Concluding Remarks

The Generalised Split-Window (GSW) algorithm is a semi-empirical algorithm that allows the estimation of LST from top-of-atmosphere brightness temperatures of two adjacent channels within the atmospheric window part of the spectrum, assuming the channel surface emissivities are known. A version of the GSW was trained for AVHRR on-board the Metop series of satellites and is currently used for operational retrieval of AVHRR-based LST (ELST, LSA-002) by the Land-SAF. To maximize the algorithm performance over a wide range of conditions, the GSW parameters are tuned for classes of satellite view angle and total column water vapour (Martins et al, 2016). The algorithm

follows closely that first prepared for SEVIRI/MSG. Despite the higher spatial resolution and global coverage provided by AVHRR observations, this sensor presents poorer spectral information when compared with SEVIRI. In particular, the cloud screening, which is based on the software maintained by the NWC SAF, had to be necessarily adapted to the available channels. Information on atmospheric water content is obtained from ECMWF operational (hourly) forecasts and in the near future, the emissivity will be based on AVHRR estimates of FVC. Since this product has not been yet implemented in the LSA SAF system, a static FVC (and therefore emissivity) is being used at the moment, taking into account the pixel land cover classification.

The AVHRR LST product is made available as a daily composite (LSA-002), aggregating all daytime and night-time LST retrievals, respectively, over a full day – a 24-hour period between 00 UTC and 23:59 UTC. The product is currently distributed with a quality flag with qualitative information on the daily night-time/daytime estimates. An example of the ELST product and respective quality flag is presented in Figure 5 and Figure 6.

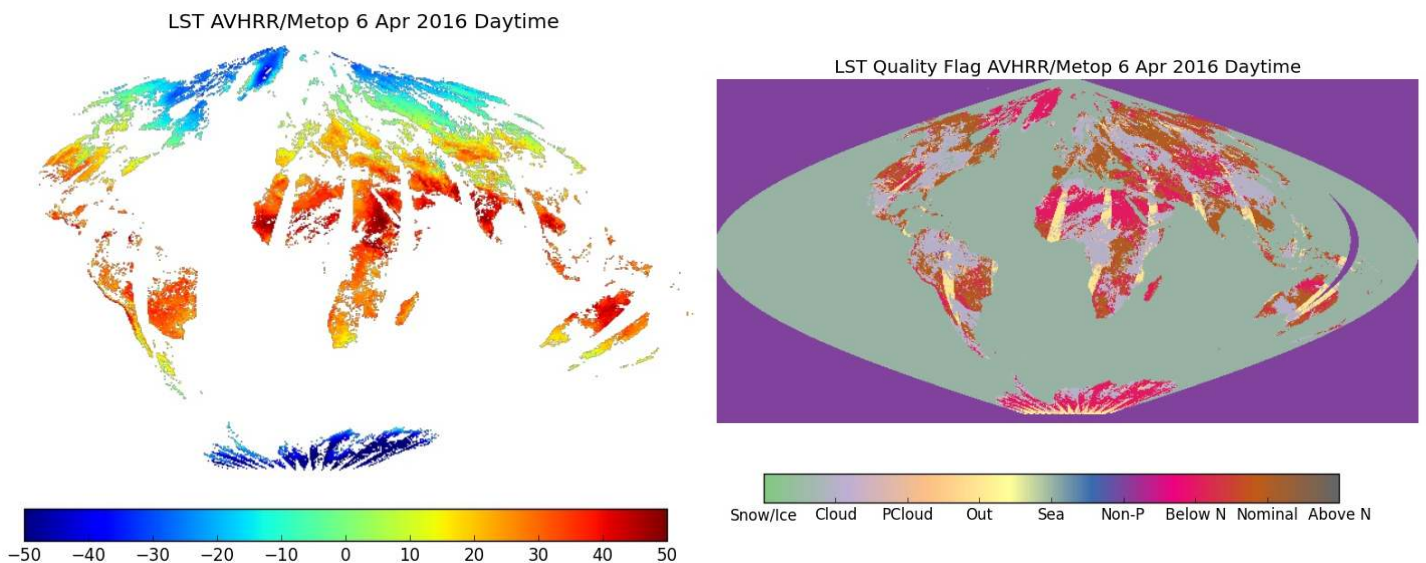
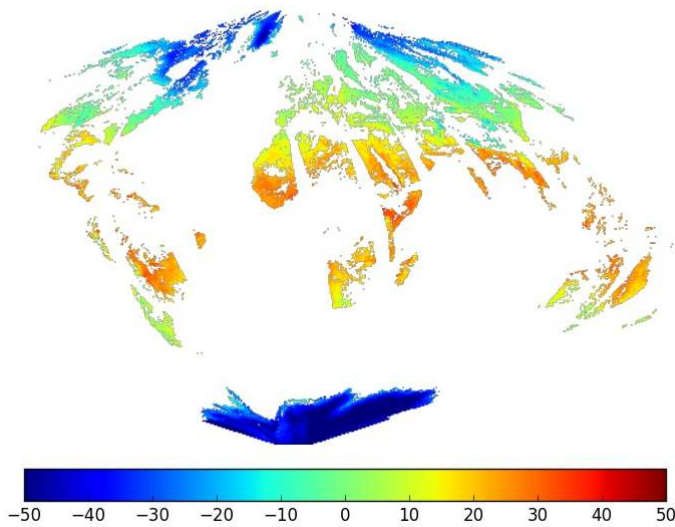
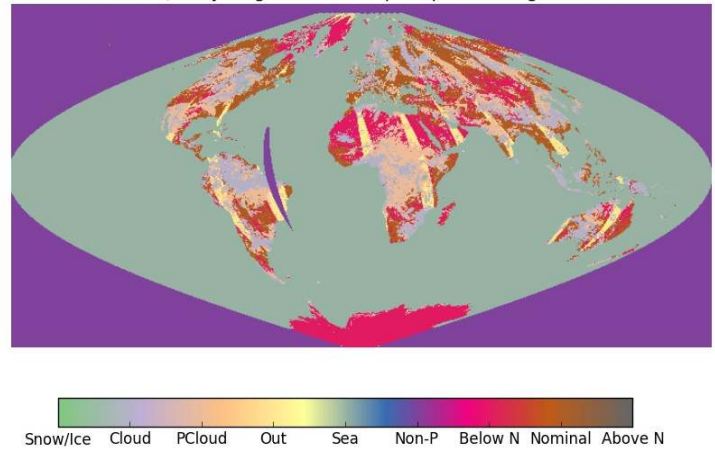


Figure 5 Example of one Daytime LST estimate (°C) and respective quality flag.

LST AVHRR/Metop 6 Apr 2016 Night-time



LST Quality Flag AVHRR/Metop 6 Apr 2016 Night-time

**Figure 6 Example of one Night-time LST estimate (°C) and respective quality flag.**

7. References

- Belward, A. S., "The IGBP-DIS global 1km land cover data set (DISCover) – proposal and implementation plans". IGBP-DIS working paper No. 13. IGBP-DIS Office, Météo-France, Toulouse, France, 61 pp, 1996.
- Berk, A., G.P. Anderson, P.K. Acharya, J.H. Chetwynd, L.S. Bernstein, E.P. Shettle, M.W. Matthew, and S.M. Alder-Golden. "MODTRAN4 Version 2 User's Manual Air Force Res. Lab.", Space Vehicles Directorate, Air Force Material Command, Hanscom AFB, MA, 2000.
- Borbás, E., S. W. Seemann, H.-L. Huang, J. Li, and W. P. Menzel, "Global profile training database for satellite regression retrievals with estimates of skin temperature and emissivity". *Proc. of the Int. ATOVS Study Conference-XIV*, Beijing, China, 25-31 May 2005, pp763-770, 2005.
- Caselles, V. and J. A. Sobrino, "Determination of frosts in orange groves from NOAA-9 AVHRR data", *Remote Sens. Environ.*, vol 29, 135–146, 1989.
- Chevallier, F., "Sampled databases of 60-level atmospheric profiles from the ECMWF analyses", Numerical Weather Prediction Satellite Application Facility Research Report [NWP SAF Res. Rep.] no. 4, Jan 2002, 2001.
- Chedin, A. N. A. Scott, C. Wahiche, and P. Moulinier, 1985, "The improved initialization inversion method: a high resolution physical method for temperature retrievals from satellites of the TIROS-N series", *J. Climate Appl. Meteor.*, vol. 24, 128-143, 1985.
- Coll, C., V. Caselles, J. M. Galve, E. Valor, R. Niclós, and J. M. Sánchez, "Evaluation of split-window and dual-angle correction methods for land surface temperature retrieval from Envisat/Advanced Along, Track Scanning Radiometer (AATSR) data", *J. Geophys. Res.*, vol. 111, D12105, doi:10.1029/2005JD006830, 2006.

- Dash, P., F. M. Göttsche, F. S. Olesen and H. Fischer, “Land surface temperature and emissivity estimation from passive sensor data: theory and practice—current trends”, *Int. J. Remote Sens.*, vol. 23, 2563–2594, 2002.
- Dybbroe, A., K.-G. Karlsson, and A. Thoss, “NWSAF AVHRR cloud detection and analysis using dynamic thresholds and radiative transfer modeling. Part I: Algorithm description”. *J. Appl. Meteor.*, **44**, 39–54, 2005.
- EUMETSAT, AVHRR Level 1b Product Guide, EUM/OPS-EPS/MAN/04/0029, v3A, 2011.
- Faysash A. and E. A. Smith, “Simultaneous land surface temperature-emissivity retrieval in the infrared split window”. *J. Atmos. Oceanic Technol.*, vol. 16, 1673-1689, 1999.
- Jiang, G.-M. and Z.-L. Li, “Split-window algorithm for land surface temperature estimation from MSG1-SEVIRI data”, *Int. J. Remote Sens.*, vol 29, 6067–6074, 2008.
- Jiménez-Muñoz, J. C. and J. A. Sobrino, “Error sources on the land surface temperature retrieved from thermal infrared single channel remote sensing data”, *Int. J. Remote Sens.*, vol 25, 999–1014, 2006.
- Masiello, G., C. Serio, S. Venafrà, G. Liuzzi, F. Göttsche, I. F. Trigo, and P. Watts, “Kalman filter physical retrieval of surface emissivity and temperature from SEVIRI infrared channels: a validation and intercomparison study”, *Atmos. Meas. Tech.*, **8**, 2981–2997, doi: 10.5194/amt-8-2981-2015, 2015.
- Martins, J. P. A., I. F. Trigo, V. A. Bento, and C. da Camara , “A Physically Constrained Calibration Database for Land Surface Temperature Using Infrared Retrieval Algorithms”, *Remote Sensing*, **8**, 808; doi:10.3390/rs8100808, 2016.
- Peres, L. F. and C. C. DaCamara, “Emissivity Maps to Retrieve Land-Surface Temperature From MSG/SEVIRI”, *IEEE Trans. Geosci. Remote Sens.*, vol. 43, pp. 1834-1844, 2005.
- Prata, A. J. “Land surface temperature derived from the advanced very high resolution radiometer and the along-track scanning radiometer: 1. Theory”, *J. Geophys. Res.*, vol. 98, 16,689– 16,702, 1993.
- Rodgers, C. D., “Inverse methods for atmospheric sounding: theory and practice”, Series on Atmospheric, Ocean and Planetary Physics, vol. 2. World Scientific, Hackensack, 238 pp., 2000.
- Seemann, S. W., J. Li, W. P. Menzel, and L. E. Gumley, “Operational retrieval of atmospheric temperature, moisture, and ozone from MODIS infrared radiances”. *J. Appl. Meteor.*, vol 42, 1072-1091, 2003
- Sobrino, J.A., M. Romaguera, “Land surface temperature retrieval from MSG1-SEVIRI data”, *Remote Sens. Environ.*, vol 92, 247–254, 2004.
- Sun, D. and R. T. Pinker, “Estimation of land surface temperature from a Geostationary Operational Environmental Satellite (GOES-8)”, *J. Geophys. Res.*, vol. 108, 4326, doi: 10.1029/2002JD002422, 2003.
- Trigo, I. F. and P. Viterbo, “Clear-Sky Window Channel Radiances: A Comparison between Observations and the ECMWF Model”, *J. Appl. Meteor.*, vol. 42, 1463–1479, 2003
- Trigo, I. F., L. F. Peres, C. C. DaCamara, and S. C. Freitas, “Thermal Land Surface Emissivity Retrieved From SEVIRI/Meteosat.”, *IEEE Trans. Geosci. Remote Sens.*, vol 46, doi: 10.1109/TGRS.2007.905197, 2008a.

- Trigo, I. F., I. T. Monteiro, F. Olesen, and E. Kabsch, “An assessment of remotely sensed Land Surface Temperature”, *J. Geophys. Res.*, vol 113, D17108, doi:10.1029/2008JD010035, 2008b.
- Wan, Z. and J. Dozier, 1996, “A generalized split-window algorithm for retrieving land surface temperature from space”, *IEEE Trans. Geosci. Remote Sens.*, vol. 34, 892–905, 1996.
- Yu, Y., J. L. Privette, and A. C. Pinheiro, “Evaluation of Split-Window Land Surface Temperature Algorithms for Generating Climate Data Records”, *IEEE Trans. Geosci. Remote Sens.*, vol. 46, doi: 10.1109/TGRS.2007.909097, 2008.

Annex - AVHRR/MetOp LST Product: LSA-002 (ELST)

The daily LST product of AVHRR/Metop follows two steps in its processing: (i) first all Product Distribution Units (PDUs) are processed; and (ii) in the second step PDUs are aggregated in order to produce the daily (day and night) files. At any given time, only the primary Metop satellite is processed.

The main flow to process one PDU follows very closely that described in the previous section for SEVIRI/MSG product. The algorithms are essentially the same, despite using input data with distinct characteristics. EM ALG is based on VCM that is a computationally efficient algorithm: EM is estimated daily, using daily values of FVC. The LST ALG then uses the most recent EM available in the system. The main steps of EM ALG execution may be described as follows:

Outer loop for EPS-AVHRR line

2 Inner loop for EPS-AVHRR column

- 2.1 select FVC input file (static or dynamical file)
- 2.2 search for land pixels, skip and flag sea pixels
- 2.3 search for FVC pixel value, skip and flag missing values
- 2.4 search for Land Cover pixel value, skip and flag missing values
- 2.5 search for snow pixels from FVC error flag and land cover file
- 2.6 compute EM for channel 4(10.3- 11.3 μm) and 5 (10.5- 11.5 μm) using FVC
- 2.7 compute EM error bars
- 2.8 identify EM confidence level and perform QC

LST ALG is based on GSW that is computationally very efficient. The major steps of LST ALG execution may be described as follows:

1 outer loop for EPS-AVHRR line

2 Inner loop for EPS-AVHRR column

- 2.1 search for land pixels, skip and flag sea pixels
- 2.2 search for valid Tb, skip and flag corrupted Tb pixels
- 2.3 search for clear sky pixels, skip and flag cloudy pixels
- 2.4 search for emissivity pixel value, skip and flag missing values
- 2.5 compute LST with GSW
- 2.6 compute LST error bars
- 2.7 identify LST confidence level and perform QC

The main flow to aggregate all PDUs gathered during a single day is based on the mapping of all pixels in each PDU onto a sinusoidal grid and on averaging LST values of multiple satellite observations falling on the same grid point; night-time and daytime overpasses are treated separately.

The major steps of EDLST ALG execution may be described as follows:

1 Loop for time (day or night)

2 Loop for each PDU

- 2.1 read SZA PDU and check solar angle corresponds to the current time cycle
- 2.2 check if the PDU overlaps the processing area
READ LST and Q-Flag PDU

dataset READ START and END TIME of sensing to calculate the reading time

dataset

READ LAT PDU

READ LON PDU

READ VZA PDU

Cycle all points of the PDU:

3 Outer loop for EPS-AVHRR line

4 Inner loop for EPS-AVHRR column

4.1 calculate the position of point in the sinusoidal grid

4.2 if the corresponding grid point is still empty, fill it with PDU point value;

else if it has already been filled with LST from a previous PDU, add the PDU value, preparing to average after all PDUs are read.

4.3 fill in gaps in the sinusoidal grid by check the correspondence of the nearest previous points to the present PDU point in the final grid by averaging LST valid values within neighbouring grid points (up to 4)

If no valid point is found, the grid point is left empty:

$(x-1,y-1)$ ---- $(x,y-1)$!These are the four
| | !points used in the interpolation
 $(x-1,y)$ ----- (x,y)

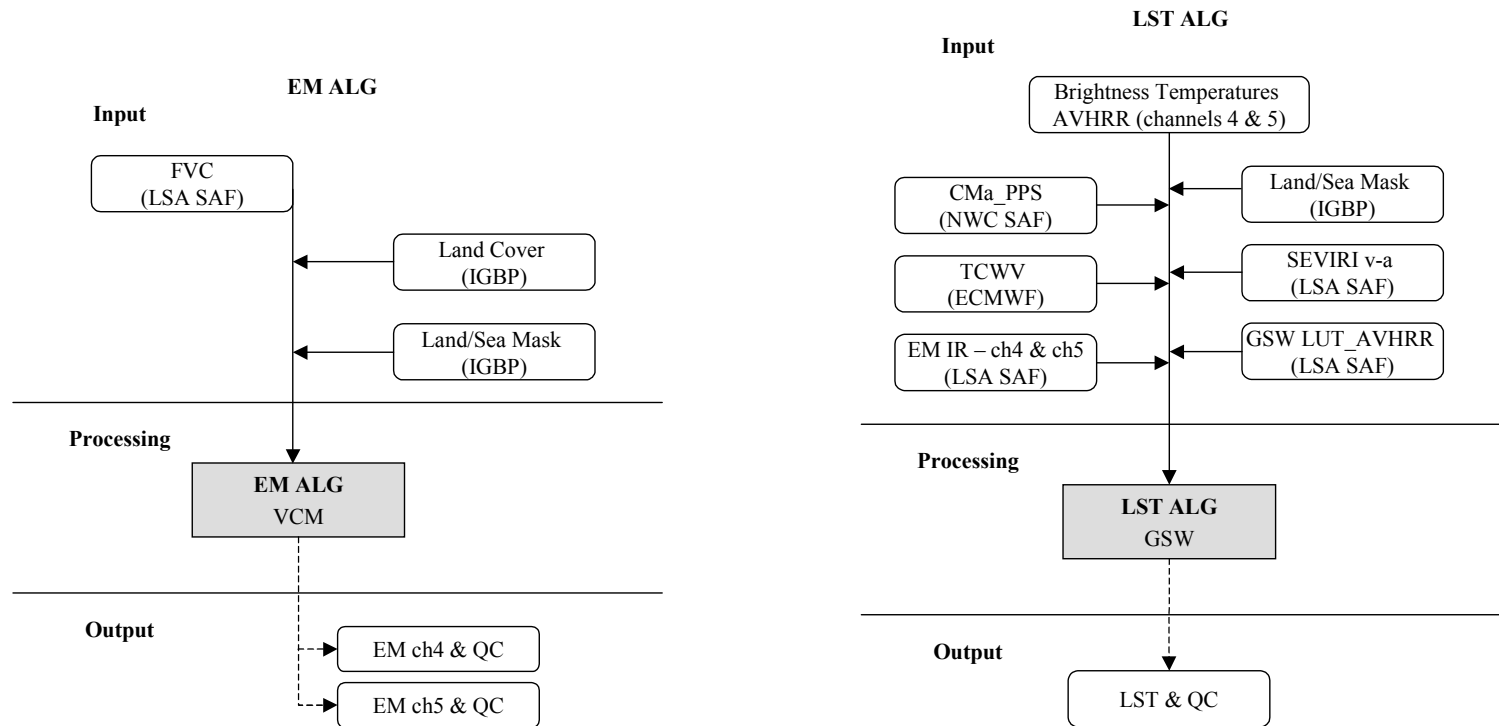


Figure 7 - Diagram of processing chain for AVHRR/Metop retrieved EM (left) and LST (right).